Experimental and numerical investigation of microstructure and mechanical behavior of titanium/steel interfaces prepared by explosive welding

Qiaoling Chu[a], Min Zhang[a]*, Jihong Li[a], Cheng Yan[b]*

[a] College of Materials Science and Engineering, Xi'an University of Technology, Xi'an, 710048, China.

[b] School of Chemistry, Physics and Mechanical Engineering, Science and Engineering Faculty, Queensland University of Technology(QUT), Brisbane, QLD 4001, Australia.

*Corresponding author: +86 02982312205 Email: chu-0080@163.com (Prof. Min Zhang);

+61 731386630 Email: c2.yan@qut.edu.au (Prof. Cheng Yan).

ABSTRACT

This paper presents a systematic study of structure and mechanical behavior of Ti/Fe explosive-bonded interfaces. The transient fluid-like behavior at the bonding zone is simulated using Smoothed Particle Hydrodynamic (SPH) numerical method. The interface is featured by a wave structure, resulted from heavy plastic deformation during the explosive welding. Melted zone resulted from the trapped jetting is surrounded by strongly deformed bulk materials. Fe_2Ti intermetallic compounds with a mixture of FeTi+Fe phases are observed in the melted zone. A reaction layer (~700nm) consisted of nano-sized FeTi grains is formed at Ti/Fe material boundary. Nanoindentation tests and fracture observation confirm the brittle nature of Fe-Ti intermetallics formed in the explosive-bonded joint. Extremely temperature accumulated near the interface leads to recovery and recrystallization in deformed grains, which can accommodate relatively large strain near the interface.

Keywords: Explosive welding; Intermetallics; Nanoindentation; Smoothed Particle hydrodynamic.

1. Introduction

Explosive welding technique has been increasingly employed to produce structural composite materials, which are difficult to be produced via conventional methods, due to potential technical problems such as metallurgical incompatibility

between claddings and base materials [1-3]. Explosive welding is generally referred as a solid state joining process, as schematically illustrated in Fig. 1. Explosive is used to compress a flyer plate towards a base plate at extremely high velocity and the joining is formed under the high pressure and high shear strain during the collision [4-7]. Laminated structures such as Ti/Fe [4, 8-9], Al/Fe [5], Cu/Ti [6], Cu/Fe [7] have been successfully produced using explosive welding.

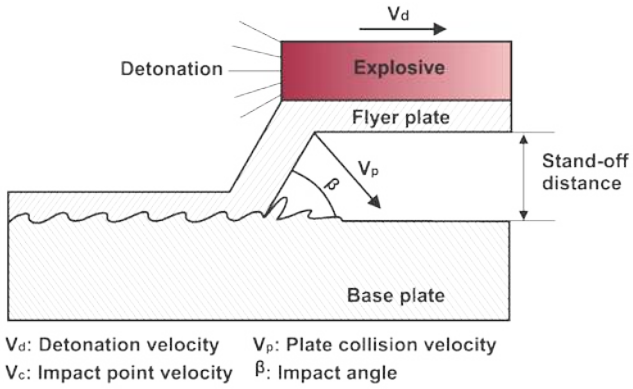

Fig.1. Schematic of explosive welding.

Generally, the joint shock wave and collision produce a wavy interface between the two plates. Kahraman et al. [6] demonstrated that the interface morphology changed from smooth bonding interface to a wavy one with increasing the explosive. The explosive detonation generates considerable amounts of heat during the welding. However, there is generally insufficient time for heat to dissipate before thermal softening occurs. This leads to partial melting at the interface and the formation of intermetallics. These intermetallics can be the source of cracking when subjected to dynamic loading [8, 10-11] or elevated temperatures [12-13]. Higher microhardness has also been observed at the interfaces compared to the base materials [4, 11]. Song et al. [10] found that the complicated (hierarchical) microstructures at the interface wave related to the enormous deformation which generated high dissipative and near-adiabatic heating. To understand the microstructures at the interface, it is critical to consider the kinetic effects of the shock wave. Due to the complexity, it is still a technical challenge to predict the microstructure

and properties at the interfaces. The relatively small size of the interface make it more difficult to conduct mechanical testing. To this end, numerical approaches are considered to be necessary, especially in predicting the shape and temperature distribution at the interface.

The waves generated by explosive welding have been numerically simulated [14-20]. Among these, Smoothed Particle Hydrodynamic (SPH) is more suitable for modeling large material distortions [18-20]. Note that under the high pressure during explosive welding, the abutting materials may behave like transient fluid-like materials [21-23].

In this work, combined experimental and numerical approaches are used to quantitatively investigate the microstructure evolution and mechanical properties of Ti/Fe explosive-bonded interface. SPH method was adopted to simulate the fluid-like behavior of abutting materials as well as the thermal transfer under high velocity impact. Scanning electron microscopy (SEM), electron backscattered diffraction (EBSD) and transmission electron microscopy (TEM) were used to characterize the microstructures. During the explosive welding, the abutting materials under high pressure behave like transient fluid-like materials [21-23]. Nanoindentation was employed to identify the mechanical properties.

2. Experimental procedures

A commercial purity Ti plate (CP Ti-1, average grain size of 20μm) was explosively bonded to a mild steel plane (Q345, average grain size of 17μm). The explosive material was an ammonium nitrate fuel oil (ANFO) mixture with the density of 0.92g/cm^3. Specimens for microstructure analysis were prepared from the central part of the joint in a plane parallel to the detonation direction and normal to explosive interface. Samples were mounted in epoxy and polished using emery papers down to 1200 grit followed by diamond polishing using 9, 3 and 1μm diamond slurries. A final surface

polishing using a 0.04μm colloidal silica suspension was done to remove the deformation zone from previous polishing steps. A JEOL 7001F SEM equipped with EBSD were used to evaluate the microstructure distribution. EBSD analysis was conducted with an accelerating voltage of 20kV, probe current of 12nA and working distance of ~20mm. TEM observations were carried out using a JEOL-2100 microscopy at 200 kV. FEI Quanta 200 3D dual beam focused ion beam (FIB) was used to prepare TEM samples. The sample was prepared perpendicularly to the Ti/Fe interface (the schematic is presented in Fig. 6a). Nanoindentation with Berkovich tip was conducted on a polished surface using a Hysitron Triboindenter TL-950 in a load control condition. Maximum load of 8000μN with a constant loading rate of 400 uNs^{-1} was applied. An array with 160 points (10×16) was set for nanoindentation test. Calibration of the tip area functions were carefully done on fused quartz with known elastic modulus (69.6 GPa±5%) and hardness (9.25 GPa±10%). The specimens for standard flat tensile tests were extracted from the central part of the joint with the longitudinal axis parallel to the detonation direction. The fracture morphology were studied by SEM. X-ray diffraction (XRD) patterns were collected on the fracture using a PANalytical X'Pert Pro diffractometer operating at 40 mV and 40 kV with Co Kα incident X-rays. Patterns were collected from 5 to 90° (2θ) at a step size of 0.0152 ° (2θ) under parallel beam geometry.

3. Numerical simulations

During the explosive welding, detonation wave propels the flyer plate with rate V_p and collision angle β towards a base plate after igniting the explosive charge, Fig. 1. Therefore, numerical modelling of the explosive welding could be simplified as an oblique impact welding process [18-19]. Simulation was carried out using LS-DYNA with SPH model. SPH is a gridless Lagrangian technique where the coordinates move with the objects. This distinct gridless feature is used to calculate spatial derivatives

associated with mesh tangling. The SPH particles are interpolation points from which values of functions and their derivatives can be estimated at discrete points in the continuum. The function values and their derivatives are found by a kernel approximation instead of being constructed from a grid [24]. Johnson-Cook constitutive equation was used to describe the mechanical behaviour of titanium and steel [25]. The relationships between the hydrostatic pressure, local specific energy, and local density were provided by Mie-Gruneisen EOS (equation of state) [18-20].

2D calculation model with total 1,500,000 particles was developed to simulate the impact welding process. The model sizes of both the flyer and base plates are 2.5 mm in thickness and 30 mm in length, respectively. The initial conditions were given in the form of the initial velocity (V_p= 955 m/s) of flyer plate and impact angle (β=13°). Time steps for the analysis were automatically computed to ensure accuracy and stability of the solution.

4. Results

4.1 Microstructures

Fig.2a displays the typical wavy structure on the cross section of Ti/Fe explosive-bonded joint. The waves have a period of ~1.0mm at a relatively constant amplitude of ~220μm. Microstructure investigation has shown elliptical melted zones in the crests. Fig. 2b shows a typical crest structure. Micro-cracks are observed in the melted zone. The numerical results of materials distribution (exhibited in Fig. 2c) reproduces the interfacial wave structure which is consistent with the experimental results. This result is essential for validating the calculations and confirming that the present modelling provides a useful insight into the actual internal plastic deformation. Jetting is formed during the impact welding, which implies that the pressure generated at the collision point exceeds the dynamic elastic limit of the materials [10, 18]. The maxmum pressure formed in the

collision zone is near 80 GPa (this contour is not displayed here). It is clear that both sides have contributed to the jetting, but the flyer plate is the main source. It seems that metals with lower density and hardness contribute much to the source of jet. As jet could remove the oxide layers from the two materials and thus results in the intmate contact, it has been considered to be an essential condition for bonding [10, 14, 21]. Although the wave morphology is in agreement with the experimental results, quantitative comparison of the wave size has not been performed as the scale of the simulation model is much smaller than the actual Ti/Fe bimetallic plates.

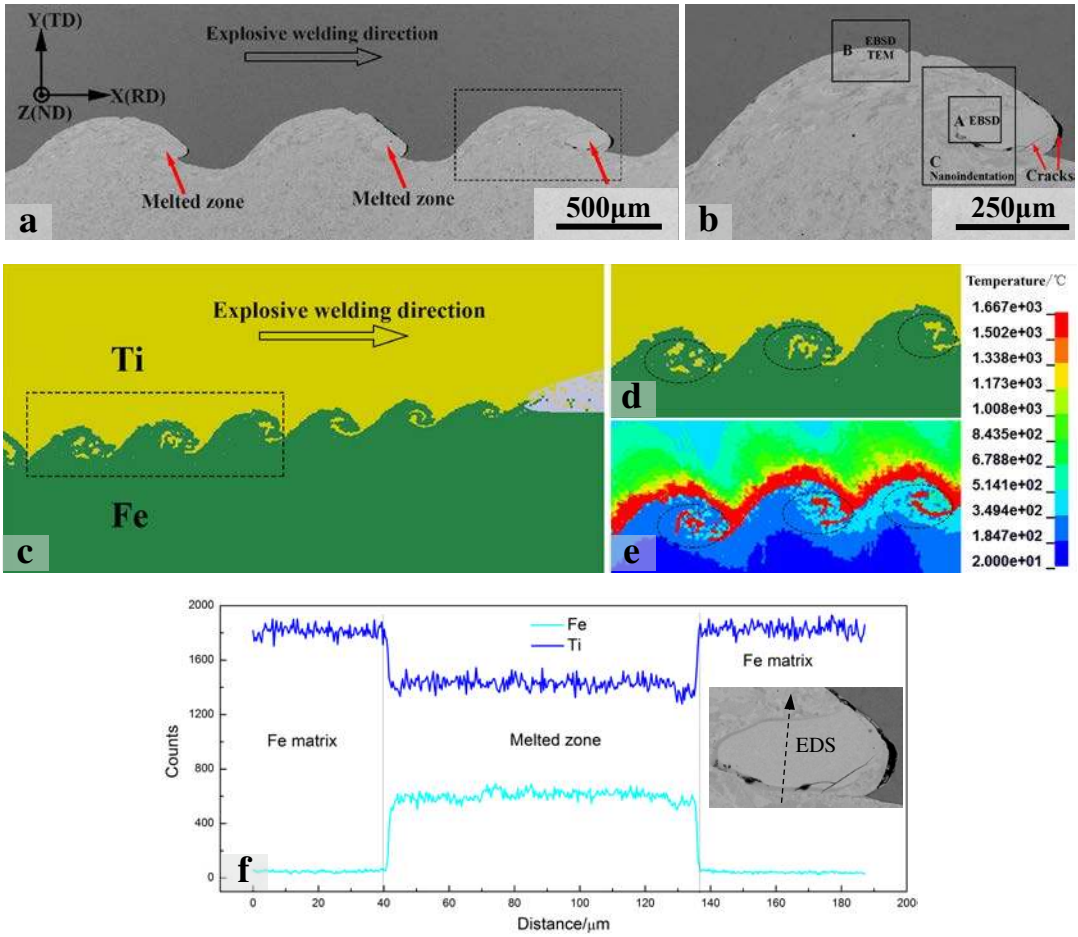

Fig. 2. Backscattered electron image on the cross sections of the Ti/Fe explosive-bonded joint. (a) Typical wave morphology with melted zone (denoted by red arrows); (b) A crest selected for further investigation; (c) Numerical results reproducing the wave structure and jetting; (d) and (e) Enlarged view of wave structure and corresponding temperature

field distribution, respectively. The melted zones are marked as dashed black circle; (f) Chemical composition distribution across the melted zone. EDS line scanning was performed along the dashed black arrow.

Enlarged view of the wave structure near the collision point reveals that vortexes are formed just behind the collision point, as displayed in Fig. 2d. Circular movement and intense stirring of the vortexes leading to strong intermixing of Ti and Fe, which eventually forms the elliptical melted zone. Fig. 2e presents high temperature distributed along the wave structure. The mechanical energy released during strong impact results to a rapid pressure boost, intense plastic deformation, friction, and shear of the two materials, which eventually converts into heat accumulation [10-11]. The vortexes exhibit high temperature (reaching the melting point of Ti), as presented red color in Fig. 2e. The melted zone predicted by simulation (dashed black circle) is quite similar to the experimental observation shown in Fig. 2a. Although the Ti/Fe material boundary corresponds to the high temperature contours, significant melted zone is only associated with the front of crest. The effect of heat accumulated at Ti/Fe interface on the microstructure evolution will be discussed in following sections.

EDS line scanning (plotted in Fig.2f) exhibits an intensely mixture of participant metals with higher percentage of Fe, which strongly validates the simulation results. Ti and Fe elements are uniformly distributed in the melted zone. Note that the percentages of Fe and Ti observed here lies in the eutectic region of Ti-Fe binary phase diagram for formation of Fe-Ti intermetallic compounds.

EBSD is employed to further investigate the microstructure in the crest selected in Fig. 2b. The results are illustrated in Fig. 3. High degree of inhomogeneity is evident in the crest. Three main phases are detected using EBSD+EDS and these phases are displayed in Fig. 3a. The melted zone is mainly consisted of Fe_2Ti intermetallics (red

color). It should be note that the formation of intermetallic phase is a common issue for most dissimilar welding systems in which steel is present. The melted zone suffers from the problems normally associated with casting, such as the formation of cavities, cracks and intermetallics. Eventually, they act as discontinuities and stress concentration points resulting in degraded mechanical properties [10, 26].

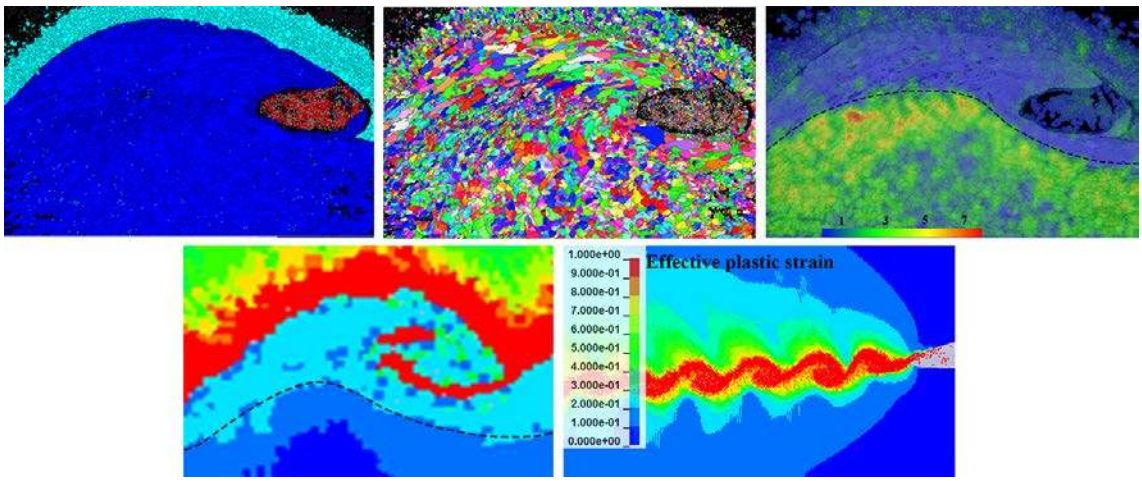

Fig. 3. EBSD images of the crest structure in Ti/Fe explosive-bonded joint. (a) Phase map indicating a Fe_2Ti rich area (red) covered by Fe (blue) and Ti (azure) matrixes; (b) Inverse pole figure (IPF) indicating strongly deformed steel grains surrounding the melted zone; (c) Strain contour calculated by EBSD software; (d) Numerical results of temperature distribution in the crest; (e) Numerical results of effective plastic strain along the interface. Interpretation of the reference temperatures see legend in Fig. 2. Step size of 1.7μm was used to collect these EBSD maps.

Inverse pole figure (IPF) map in Fig. 3b indicates finer grains formed in the melted zone. Trace of deformation and elongation is evident in the Fe matrix. These grains are curved inside the crest and imitated well the rotational character of the material displacement during the wave formation. Meanwhile, the effective plastic strain contour extracted from the numerical simulation (as displayed in Fig. 3e) depicts dramatic strain along the interface. Therefore, the experiment and numerical results confirm the fluid-

like behavior of the materials under the impact load. Furthermore, some finer Fe grains are observed surrounding the melted zone.

Strain is calculated and the result is presented in Fig. 3c. As presented in Fig. 3e, the temperature decreases with the increase of the distance from the interface. It is obvious that the regions accumulating higher temperature (349-1667℃) present lower strain (~1%). The maximum strain (~7%) is formed in regions with a distance of ~250μm from the Ti/Fe interface (indicated by black dashed curve). Under that curve, the strain level decays as a function of the spacing from the joining interface, which is consistent with the prediction in [10]. The plastic strain (displayed in Fig. 3e) decreases with the distance to the joining interface, in the same trend with the evaluated by EBSD. Generally, dynamic recovery and recrystallization will occur in deformed structure when subjected to elevated temperature [27] and they will result in the material softening. Therefore, the above results imply that the microstructure evolution probably occur during the welding.

Fig. 4a shows the enlarged view of the region (marked A in Fig. 2b) including melted zone and Fe matrix. A transition layer with around width of 8μm is formed adjacent to the Fe matrix in the melted zone. This transition zone is referred as “melted zone I” and the rest of the melted zone as “melted zone II”. Fig. 4b shows the EDS line profiles of Ti and Fe elements. Ti content in melted zone I exhibits a gradual decreasing trend towards the Fe matrix, which is most likely the diffusion between melted zone II and Fe matrix. It is well known that plastic deformation will lead to an increase in defect density [28]. This enhanced defect density could cause a rise in diffusion rate. Melted zone II displays uniform composition distribution. EBSD point analysis (illustrated in Fig. 4c) is performed to identify the crystal structure dominant in these regions. Fe_2Ti kikuchi pattern is identified in melted zone II. Melted zone I is consisted of two crystal structures, FeTi and Fe (only FeTi kikuchi pattern presented here). A closer analysis is performed

by EBSD mapping. Fig. 4d and 4e present the relevant inverse pole figure (IPF) maps in melted zone I and II, respectively. It is pronounced that the melted zone I exhibits much finer grains with an average value of ~500nm, whereas melted zone II has much coarser ones with an average value of ~1000nm. Despite the different grain size, some nano-size grains are observed in these two regions, which is probably due to intense shear force and rapid cooling rates in the melted zone [10, 26, 29]. EBSD phase map (Fig. 4f) presents Fe_2Ti intermetallics (red color) dominant in melted zone II. However, the phase map in melted zone I exhibits significant mixture of FeTi and Fe phases (images were not presented here). It is probably due to the similar crystalline parameters of FeTi and Fe, which makes it difficult to distinguish each other. Similarly, small amount of FeTi+Fe mixture (blue+yellow) with ultrafine grain size is also observed in the melted zone II (Fig.4f).

ultrafine grain size was also observed in the melted zone II (Fig.4f).

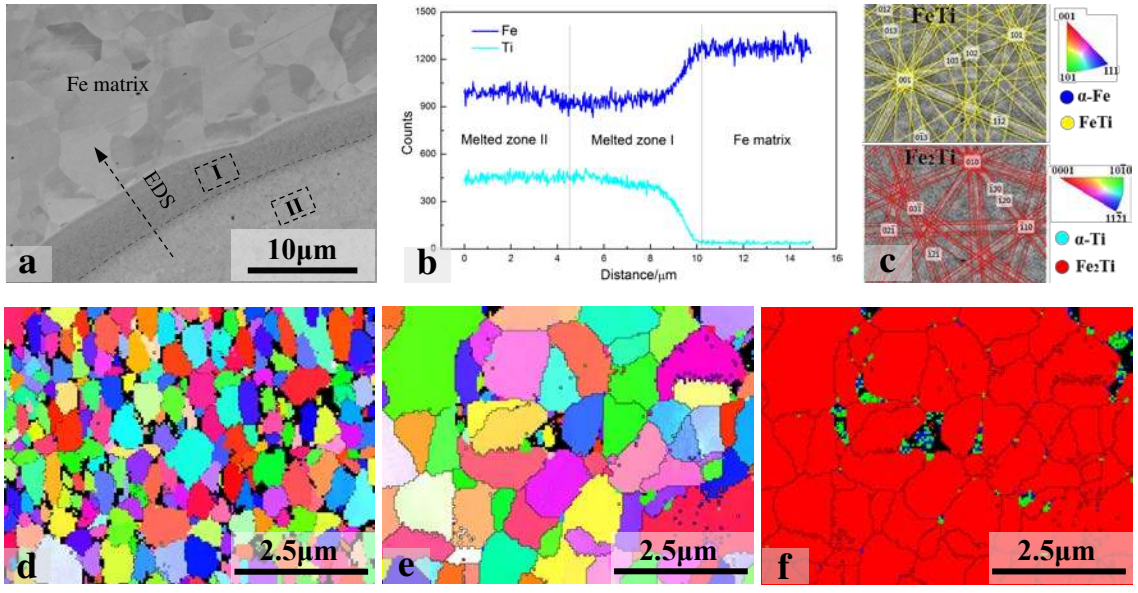

Fig. 4. EBSD results in melted zone. (a) Secondary electron micrograph of the melted zone. The image is an enlarged view of region marked A in Fig. 2b. (b) Chemical composition distribution across melted zone I; (c) Kikuchi patterns of FeTi and Fe_2Ti crystalline structures in melted zone I and II, respectively; (d) and (e) EBSD inverse pole

figures (IPFs) of melted zone I and II, respectively. Much finer grains were identified in melted zone I. (f) EBSD phase map of melted zone II illustrating the dominant phase of Fe_2Ti. Step size of 50nm was used to collect the EBSD maps.

Using crystal orientations obtained by EBSD technique the pole figure (PF) of the Fe_2Ti phase is determined (images were not presented here). However, no strong orientation relationship is found. It is probably due to the strong stirring and high cooling rate in the melted zone, which interrupt the potential texture formation. Moreover, hard particles are likely to have an effect on the development of random orientations (high hardness revealed in the melted zone in Fig. 8) [28].

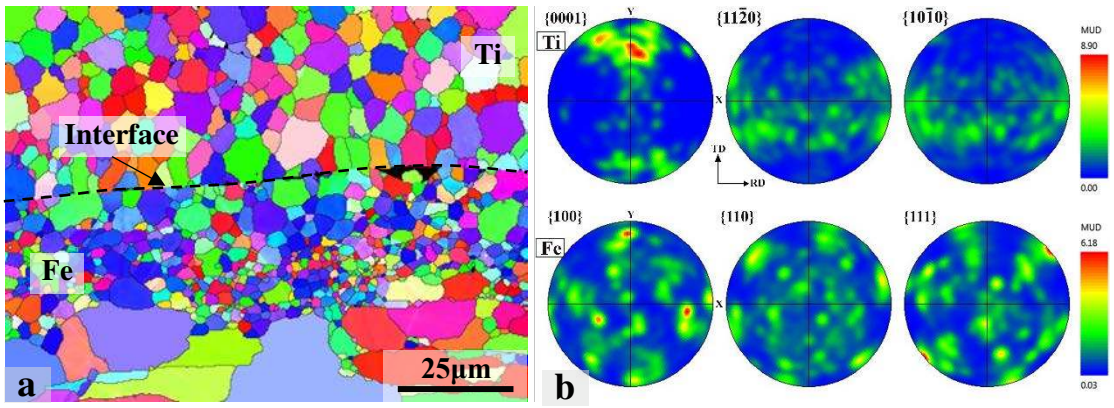

Fig. 5. EBSD results at Ti/Fe interface. (a) Inverse pole image (IPF) map of region marked B in Fig. 2b; (b) Pole image (PF) of Ti revealing the texture close to the ideal orientation specified by the Euler angles (270°, 60°, 0°) orientation [30]; Pole image (PF) of Fe revealing weak {110}<001> texture; Step size of 280nm was used to collect the EBSD maps.

As previously discussed, recovery and recrystallization probably occur at Ti/Fe interface. Observation at higher magnification in the region marked B in Fig. 2b is shown in Fig. 5. EBSD inverse pole figure (IPF) map is shown in Fig. 5a, which indicates distinct recrystallized structure at both sides. At Ti side, uniform equiaxed structure with an average grain size of ~8μm is formed. However, it appears more heterogeneous at Fe side

with the grain size ranging from 1μm to 25μm. As referring to the numerical results in Fig. 2e, this characteristics is probably due to the severe temperature gradient at Ti/Fe interface. Similar results were also reported by Paul et al. [29] where apparent fine-structure is well visible inside the crests. The equiaxed Fe grains are limited to an area within about 50μm from the interface. With the distance increasing, coarse grains are observed. Elongation remained in these grains implies only recovery occurred. Referring to the numerical results, the adiabatic temperature rise during the impacting resulted in dynamic recrystallization at the interface, which is similar as reported in UAM (ultrasonic additive manufacturing) joints [28].

Fig. 5b shows the EBSD pole figures (PFs) of Ti and Fe matrixes, respectively. For the titanium, it is close to the ideal orientation specified by the Euler angles (270°, 60°, 0°) orientation and the corresponding fibre of c direction, denoted as <c>-fibre in pole figures [30]. This texture is frequently observed in hcp materials under ECAP (equal-channel angular pressing) passes [31]. ECAE is a special industrial process employed to realize the simple shear in metal-working. The simple shear can be considered a 'near ideal' deformation method for structure and texture formation [32]. Since shear deformation is dominated at the abutting materials under highly oblique impact [10], similar texture is determined in this study. For the Fe matrix, a weak Goss texture ({110}<001>) is identified. It is well established that Goss grains originate at shear bands in {111}<112> deformed matrices, and to a lesser extent at shear bands in {111}<110> and {112}<110> deformed matrixes [33, 34].

As referring to Ti/Fe material interface (Fig. 5a), it presents sharp transition, which seems that there is no mechanical mixing between Ti and Fe materials. However, numerical results reveal high temperature in this region (Fig. 2e and Fig. 3d). In order to determine the microstructure distribution between Ti and Fe matrix, TEM lamella is

prepared (displayed in Fig. 6a and b). Fig. 6c illustrates the Ti/Fe material interface using TEM bright field contrast and corresponding diffraction patterns. A reaction layer with an average width of ~800nm is observed. This layer is composed of very fine grains (nano-size) with diameter rarely exceed 200nm. Previous investigations [10, 29] also reported similar structure at Ti/Fe explosive-bonded interface. Selected area diffraction pattern determines FeTi intermetallics dominant in this region. Unlike the melted zone in the crest, this reaction layer presents sound bonding with the adjacent materials. Therefore, the formation of thin reaction layer between abutting materials is probably essential to obtain proper explosive welded joint [29].

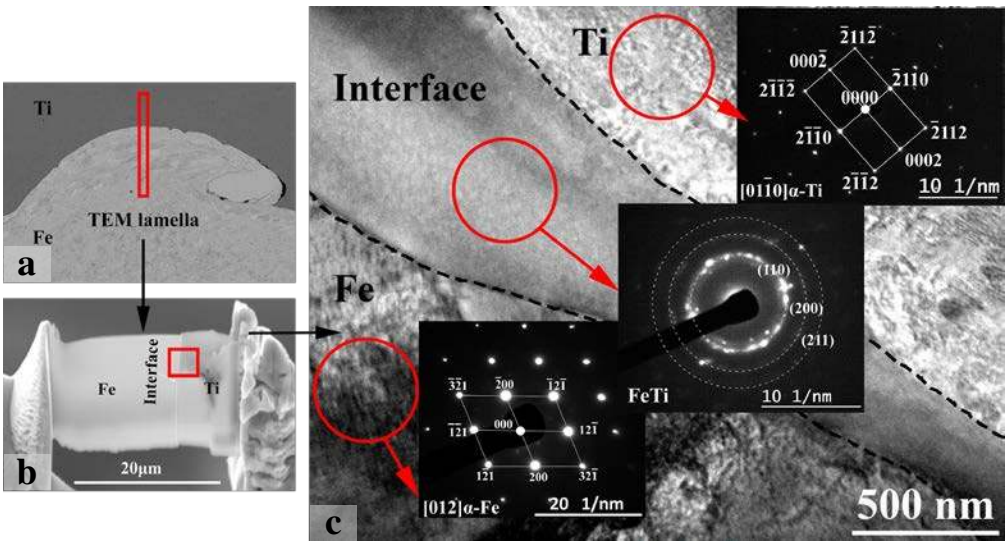

Fig. 6 TEM results at Ti/Fe interface. (a) TEM sample cut perpendicular to the Ti/Fe interface and (b) prepared by FIB; (c) TEM bright field image showing formation of nano-grained intermetallic phase in the interface region. The regions from which the diffraction patterns were collected are highlighted by red circles. The size of the selected area aperture used is ~200nm.

4.2 Nanoindentation results

In order to determine mechanical properties in melted zone, nanoindentation tests are performed. Grid with total 160 points, as outlined by dashed black rectangle in Fig. 7a, is subjected to nanoindentation testing. Fig. 7b shows the corresponding nano-

hardness mapping. Melted zone II exhibits a relatively uniform hardness contour with the values restricted within a range of 9-13GPa (green colour). Some triangle indents loaded inside the melted zone I are marked by dashed red circles, as presented in Fig. 7a. These indents reveal higher nano-hardness (17GPa-22GPa) as displayed red colour in Fig. 7b. Fe matrix presents much lower nano-hardness with an average hardness of 2.4GPa (blue colour). Furthermore, the regions surrounding the melted zone presents lower hardness (deep blue) compared to the Fe matrix. It is most likely due to the recrystallization which has the softening effect on the microstructure [11, 35]. These recrystallized grains surrounding the melted zone could arrest the cracks propagated from the brittle melted zone [10]. Fig. 7c displays representative Berkovich impressions (marked by dashed white rectangle in Fig. 7a). These impressions are located in Fe matrix (A), melted zone I (B) and melted zone II (C), respectively. Different mechanical response of these regions is presented. It is evident that melted zone reveals much smaller indents than Fe matrix. The corresponding force-depth curves (P-h) are displayed as inset in Fig. 7c. The maximal indenter displacement (h_{max}) upon a peak load of 8000μN is much larger for Fe matrix (399.5nm) compared to that of melted zone I (160.7nm) and melted zone II (196.0nm).

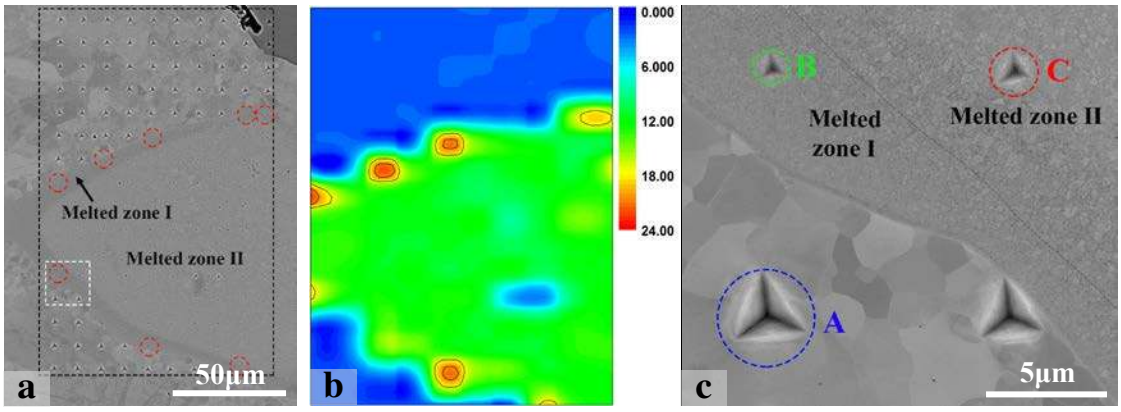

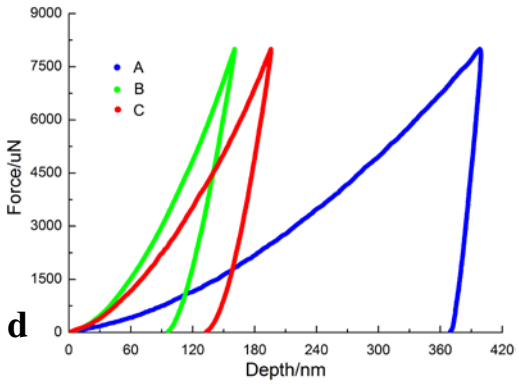

Fig. 7 Nanoindentation tests on cross section of Ti/Fe joint (this regioin is an enlarged view of C in Fig. 2b). (a) Backscattered electron image highlighting the nanoindentation area. Some of the indents located in melted zone I were are marked by dashed red circle; (b) 2D nano-hardness mapping presenting pronounded hardness distribution; (c) Backscattered electron image of impressions; (d) Force-depth (P-h) curves for indents marked A-C.

The deviation of the indentation properties of different regions is obviously attributed to the phase properties. The presence of stronger and stiffer Fe-Ti intermetallics lead to an increase in the constraint to localized plastic deformation of the material during the nano-hardness test. Similar results were also obtained by Rosenthal et al. [3] and Venkateswaran et al. [36] in which higher nano-hardness is revealed due to the presence of intermetallic phases. Furthermore, the higher hardness revealed in melted zone I is probably due to the ultra-fine structure formed in this region.

4.3. Fracture analysis

The tensile tests are conducted to evaluate the mechanical properties of the Ti/Fe explosion-welded joint. An ultimate tensile strength of 540MPa is revealed. Since these two materials exhibit significant difference in strength and ductility, Ti plate fails at first and then the explosive interface is separated. With the increasing of displacement, Fe plate fractures ultimately. Here, the explosive interface (at titanium side) is selected for investigation and the results are presented in Fig. 8.

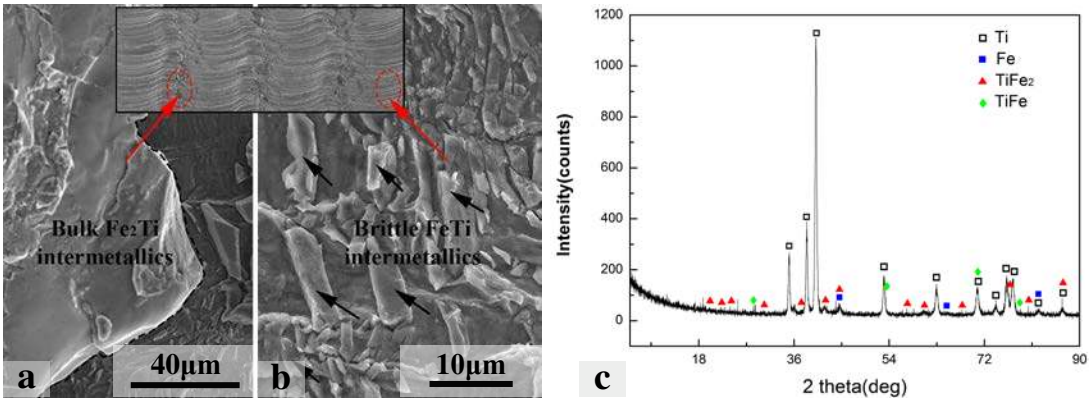

Fig. 8. Secondary electron micrography of explosive interface showing (a) melted zone with smooth morphology and (b) fragile rods at titanium side; (c) X-ray diffraction results on the explosive interface.

Bulk fragments with smooth morphology are presented on the fracture (Fig. 8a). EDS analysis reveals that this structure corresponds to Fe_2Ti intermetallics. Therefore, it is most likely to be the melted zone. Another pronounced fracture displayed in Fig. 8b is the fragile rods which are detected rich in FeTi phase. As regard to the morphology and distribution, they are highly likely to be the thin FeTi layer (Fig. 6c) formed at Ti/Fe material boundary. Fig.8c displays the X-ray diffraction pattern on the explosive interface, which confirms the presence of Fe_2Ti and FeTi.

5. Discussion

The mechanism of explosive welding has been earlier addressed by Bahrani et al. [21] in which the impacting plates in the collision zone behave in a similar manner as liquids of lower viscosity. Fig. 9a-d present the simulation results of wave formation with the corresponding joining mechanism insets developed by Bahrani et al [21]. The typical wavy interface is controlled by an oscillation in the jet flow. Bahrani et al. [21] proposed that the flyer plate could divide into a re-entrant jet and a salient jet. The pressure produced at the stagnation point (S) of the divided jet must be of sufficient magnitude to exceed the dynamic elastic limit of the material [1,10-11]. The base plate deforms under the stagnation point and consequently a crest is formed (Fig. 9a). When the re-entrant jet

is completely choked, the stagnation point moves from the trough to the crest (Fig. 9b). The high pressure at the stagnation point will depress and elongate the crest so that a forward trunk is formed. Part of the re-entrant jet enters the cavity under the trunk causing a vortex (Fig. 9c). When a vortex is produced, the displacement boundary conditions around it lead to a circular movement and intense stirring. Besides forming a vortex in the first wave, the re-entrant jet sweeps the surface of the base plate ahead of the first wave and then produces another crest as shown in Fig. 9d. It is then evident that removal of surface oxide layers by the jet is the necessary first step to bring the materials into intimate contact [10, 14, 21]. The elongated grains (Fig. 3b) which are strongly curved inside the crest characterize the rotational movement of the material during the wave formation.

Extremely impact at the collision points eventually leads to heat generation, as presented in Fig. 9e. When the wave is formed, the temperature increase is dominant with respect to transferring the heat away from the collision point [29]. Therefore, the latest wave structure exhibits much higher temperature contour than the earlier ones. Since the process is extremely fast, there is no time for the heat to be transferred away from the interface. Therefore, any increase of temperature and melting is local. Here, high temperature (reaching melting point of Ti) is concentrated in vortex and Ti/Fe material boundary. Local melting could origin from trapped jet energy and dissipative deformation heating [10]. In this study, the melted zone involved in the crest is much more obvious than the reaction layer formed at Ti/Fe interface. It then seems that the latter mechanism is of lower relevance compared to direct melting through the jet energy captured in the vortex [10-11, 21]. Indeed, the dissipative deformation heating plays an important role in the recovery and recrystallization occurred at Ti/Fe interface.

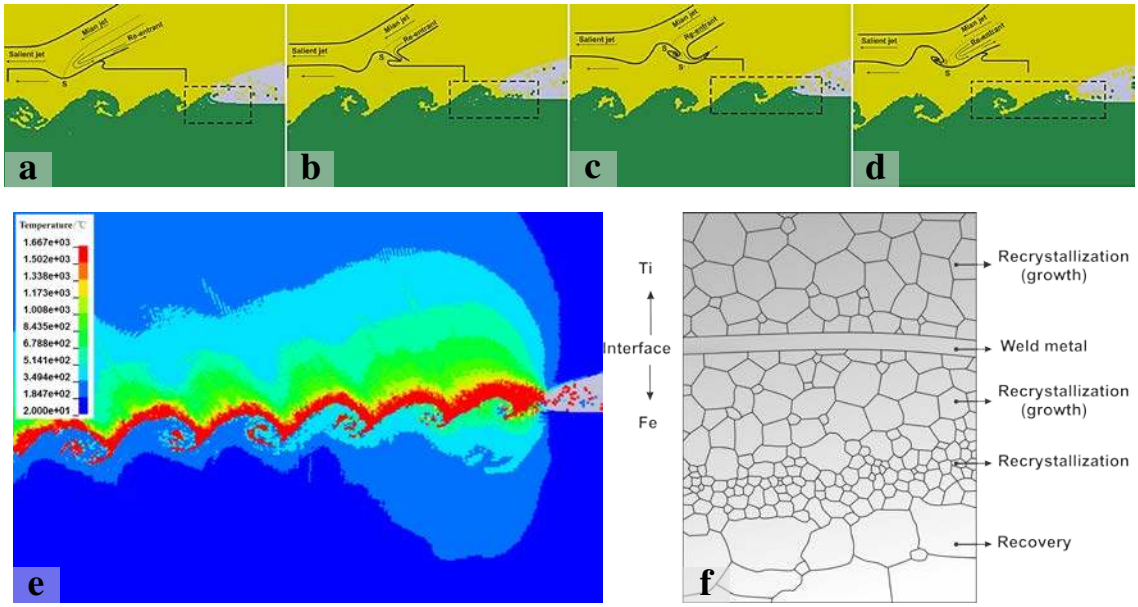

Fig. 9 (a)-(d) Formation of wave structure during explosive welding simulation. (a) Formation of jet; (b) Crest interfered by jet; (c) Jet trapped in the cavity of crest; (d) Completion of a wave structure.(e) Temperature distribution during explosive welding; (f) Schematic diagram of microstructure distribution along the Ti/Fe interface.

The history of dramatic temperature changing during the impacting process can be used to elucidate the microstructure evolution mechanism at Ti/Fe interface. Considering the heat-exchange, the difference in temperature distribution may be interpreted by the following equation [37]:

$$C_V \rho \frac{\partial T}{\partial t} = \tau_{ij}\gamma_{ij} - k\frac{\partial^2 T}{\partial x^2} \quad (1)$$

Where, τ_{ij} is the equivalent shear stress, $\tau_{ij}\gamma_{ij}$ is the plastic shearing deformation power, $k\frac{\partial^2 T}{\partial x^2}$ is the energy loss rate due to the thermal conduction, C_V, ρ, T,k, t are the specific heat, density, temperature, thermal conductivity and time, respectively. Here, values of $\tau_{ij}\gamma_{ij}$ is assumed the same for these two materials. Due to the lower conductivity, the energy-loss rate of Ti caused by thermal conduction is less than that of the steel. Therefore, more energy accumulates at Ti side. This is agreed well with the numerical results. Based on the knowledge of dynamic recrystallization [34-35], new

grains nucleate and grow within the deformed grains will occur when the temperature higher than $0.4T_m$ (T_m is the melting point). However, due to the high dislocation density increasing the driving force for recrystallization in deformed structure, the critical recrystallization temperature may be lower. The recrystallization appears as a result of the heat transfer between the melt and the heavily deformed materials. Steep temperature gradient at Fe side is responsible for the pronounced trace of deformation-recovery-recrystallization (Fig. 9f). These grains experience the following processes: dislocations accumulate to form elongated structures, cell structure break up to form subgrains, and subgrains rotate and finally form recrystallized grains [38]. Since the temperature is higher at the interface, the grains which are adjacent to the interface have undergone grain growth. As similar results observed in solid bond joints, the recrystallization at the interface will cause a reduction in the interfacial energy [28, 39]. Although Fe-Ti intermetallic formed in the explosive-bonded exhibit quite high hardness and brittle nature, the recrystallized structure around it will compensates local strain peaks (as low strain rate displayed near the interface in Fig. 3c) and does not allow for easy crack propagation.

6. Conclusion

Quantitative analyses of the microstructure evolution in Ti/Fe explosive-bonded joint is performed using both experimental and numerical approaches. Ti/Fe interface is featured by a wavy structure with melted zones embedded in the crests. SPH simulations indicate the fluid-like behavior of abutting materials. It is found that extremely rapid temperature increase followed by high cooling rates at the interface is responsible for the deformation-recovery-recrystallization. The melted zone mainly resulted from the trapped jet is dominated by Fe_2Ti intermetallics surrounded by a mixture of FeTi+Fe. Nano-size FeTi intermetallics are observed at Ti/Fe interfaces. Correlation between the

microstructure and mechanical properties is established via nanoindentation tests. Although high hardness has been observed in the melted zone, the recrystallized structure may accommodate localized strain. The formation of melted region between abutting materials has been confirmed in this study.

Acknowledgements

This work was supported by the National High Technology Research and Development Program of China (Grant No.2013AA031303), the Doctorial Innovation Found (Grant No. 207-002j1405) and Doctorial Cultivation Found of Xi'an University of Technology. Cheng Yan acknowledges the support from Australian Research Council Discovery fund (DP150101717). The authors also wish to acknowledge the High Performance Computing (HPC) and CARF at QUT for access to their facilities.

References

[1] S.A.A Akbari Mousavi, P. Farhadi Sartangi. Experimental investigation of explosive welding of cp-titanium/AISI 304 stainless steel, Mater. Des. 30 (2009) 459-468.

[2] F. Findik. Recent developments in explosive welding, Mater. Des. 32 (2011) 1081-1093.

[3] I. Rosenthal, A. Miriyev, E. Tuval, A. Stern, N. Frage. Characterization of explosion-bonded Ti-alloy/steel plate with Ni interlayer, Metallogr. Microstruct. Anal. 3 (2014) 97-103.

[4] N. Kahraman, B. Gulenc, F. Findik. Joining of titanium/stainless steel by explosive welding and effect on interface, J. Mater. Process. Technol. 169 (2005) 127-133.

[5] J.H. Han, J.P. Ahn, M.C. Shin. Effect of interlayer thickness on shear deformation behavior of AA5083 aluminum alloy/SS41 steel plates manufactured by explosive welding, J. Mater. Sci. 38 (2003) 13-18.

[6] N. Kahraman, B. Gulenc. Microstructural and mechanical properties of Cu-Ti plates bonded through explosive welding process, J. Mater. Process. Technol. 169 (2005) 67-71.

[7] A. Durgutlu, B. Gülenc, F. Findik. Examination of copper/stainless steel joints formed by explosive welding, Mater. Des. 26 (2005) 497–507.

[8] P. Manikandan, K. Hokamoto, M. Fujita, K. Raghukandan, R. Tomoshige. Control of energetic conditions by employing interlayer of different thickness for explosive welding of titanium/304 stainless steel, J. Mater. Process. Technol. 195 (2008) 232-240.

[9] M.X. Xie, L.J. Zhang, G.F. Zhang, J.X. Zhang, Z.Y. Bi, P.C. Li. Microstructure and mechanical properties of CP-Ti/X65 bimetallic sheets fabricated by explosive welding and hot rolling, Mater. Des. 87 (2015) 181-197.

[10] J. Song, A. Kostka, M. Veehmayer, D. Raabe. Hierarchical microstructure of explosive joints: example of titanium to steel cladding, Mater. Sci. Eng. A 528 (2011) 2641-2647.

[11] M. Gloc, M. Wachowski, T. Plocinski, K.J. Kurzydlowski. Microstructural and microanalysis investigations of bond titanium grade1/low alloy steel st52-3N obtained by explosive welding, J. Alloys Compd. 671 (2016) 446-451.

[12] S.A.A. Akbari Mousavi, P. Farhadi Sartangi. Effect of post-weld heat treatment on the interface microstructure of explosively welded titanium-stainless steel composite, Mater. Sci. Eng. A 494 (2008) 329-336.

[13] Q.L. Chu, M. Zhang, J.H. Li, Q. Jin, Q.Y. Fan, W.W. Xie, H.L. Luo, Z.Y. Bi. Joining of CP-Ti/Q345 sheets by Cu-based filler metal and effect on interface, J. Mater. Process. Technol. 225 (2015) 67-76.

[14] A. A. Akbari Mousavi, S.T.S. Al-Hassani. Numerical and experimental studies of the mechanism of the wavy interface formations in explosive/impact welding, J. Mech. Phys. Solids 53 (2005) 2501-2528.

[15] A. A. Akbari Mousavi, S.T.S. Al-Hassani. Finite element simulation of explosively-driven plate impact with application to explosive welding, Mater. Des. 29 (2008) 1–19.

[16] W. Wang, Y. Huang, M. Grujicic. Study of impact-induced mechanical effects in cell direct writing using smooth particle hydrodynamic method, J. Manuf. Sci. Eng. 130 (2008) 1-9.

[17] Y.X. Wang, H.G. Beom, M. Sun, S. Lin. Numerical simulation of explosive welding using the material point method, Int. J. of Impact Eng. 38 (2011) 51-60.

[18] X. Wang, Y.Y. Zheng, H.X. Liu, Z.B. Shen, Y. Hu, W. Li, Y.Y. Gao, C. Guo. Numerical study of the mechanism of explosive/impact welding using smoothed particle hydrodynamics method, Mater. Des. 35 (2012) 210-219.

[19] K. Tanaka. Numerical studies on the explosive welding by smoothed particle hydrodynamic (SPH), AIP Conference Proceedings 955 (2007) 1301-1304.

[20] A.D. Monaco, S. Manenti, M. Gallati, S. Sibilla, G. Agate, R. Guandalini. SPH modeling of solid boundaries through a semi-analytic approach, Eng. Appl. Comp. Fluid Mech. 5 (2011) 1–15.

[21] A.S. Bahrani, T.J. Black, B. Crossland. The mechanics of wave formation in explosive welding, Proc. R. Soc. A 296 (1967) 123-136.

[22] V.G. Petushkov. Physical interpretation of explosion welding near its lower boundary, Combustion, Explosion, and Shock Waves, 36 (2000) 771-776.

[23] H. El-Sobky, T.Z. Blazynski. Experimental investigation of the mechanics of explosive welding by means of a liquid analogue. In: Proceedings of the Fifth

International Conference on High Energy Rate Fabrication, Denver, Colorado, 4 (1975) 1-21.

[24] M.B. Liu, G.R. Liu. Smoothed particle hydrodynamics (SPH): an overview and recent developments, Arch. Comput. Methods Eng. 17 (2010) 25-76.

[25] G.R. Johnson, W.H. Cook. A constitutive model and data for metals subjected to large strains, high strain rates and high temperatures. In: Proceedings of the 7th International Symposium on Ballistics, The Hague, Netherlands; 19-21 April, 1983.

[26] M. Abbasi, M. Dehghani, H.U. Guim, D.I. Kim. Investigation of Fe-rich fragments in aluminium-steel friction stir welds via simultaneous Transmission Kikuchi Diffraction and EDS, Acta Mater. 117 (2016) 262-269.

[27] H.J. McQueen. Development of dynamic recrystallization theory, Mater. Sci. Eng. A 387-389 (2004) 203-208.

[28] N. Sridharan, P. Wolcott, M. Dapino, S.S. Babu. Microstructure and texture evolution in aluminium and commercially pure titanium welds fabricated using ultrasonic additive manufacturing, Scr. Mater. 117 (2016) 1-5.

[29] H. Paul, J. Morgiel, T. Baudin, F. Brisset, M. Prazmowski, M. Miszczyk. Characterization of explosive weld joints by TEM and SEM/EBSD, Arc. Metall. Mater. 59 (2014) 1129-1136.

[30] K. Kowalczyk-Gajewska, K. Sztwiertnia, J. Kawalko, K. Wierzbanowski, M. Wronski, K. Frydrych, S. Stupkiewicz, H. Petryk. Texture evolution in titanium on complex deformation paths: Experiment and modelling, Mater. Sci. Eng. A 637 (2015) 251-263.

[31] P. Mehrotra, T.M. Lillo, S.R. Agnew. Ductility enhancement of a heat-treatable magnesium alloy. Scr. Mater. 55(2006) 855-858.

[32] V.M. Segal. Materials processing by simple shear, Mater. Sci. Eng. A 197 (1995) 157-164.

[33] J.T. Park, J.A. Szpunar. Evolution of recrystallization texture in nonoriented electrical steels, Acta Mater. 51 (2003) 3037-3051.

[34] Y.H. Sha, C. Sun, F. Zhang, D. Patel, X. Chen, S.R. Kalidindi, L. Zuo. Strong cube recrystallization texture in silicon steel by twin-roll casting process, Acta Mater. 76 (2014) 106-117.

[35] J.J. Jonas, X. Quelennec, L. Jiang, E. Martin. The Avrami kinetics of dynamic recrystallization, Acta Mater. 57 (2009) 2748-2756.

[36] P. Venkateswaran, Z.H. Xu, X.D. Li. Determination of mechanical properties of Al-Mg alloys dissimilar friction stir welded interface by indentation methods, J. Mater. Sci. 44 (2009) 4140-4147.

[37] Y. Yang, Z. Xinming, L. Zhenghua, L. Qingyun. Adiabatic shear band on the titanium side in the Ti/mild steel explosive cladding interface, Acta Mater. 44 (1996) 561-565.

[38] Y. Yang, B.F. Wang, J. Xiong, X.Y. Yang, Y. Zeng, Z.P. Chen. Adiabatic shear bands on the titanium side in the titanium/mild explosive cladding interface: experiments, numerical simulation, and microstructure evolution, Metall. Mater. Trans. A 37(2006) 3131-3137.

[39] E. Mariani, E. Ghassemieh. Microstructure evolution of 6061 O Al alloy during ultrasonic consolidation: An insight from electron backscatter diffraction, Acta Mater. 58 (2010) 2492-2503.